# Reflection of Planetary Waves in Three-Dimensional Tropospheric Flows

GUDRUN MAGNUSDOTTIR

*Department of Earth System Science, University of California, Irvine, Irvine, California*

PETER H. HAYNES

*Centre for Atmospheric Science, Department of Applied Mathematics and Theoretical Physics, University of Cambridge, Cambridge, United Kingdom*

(Manuscript received 24 November 1997, in final form 17 April 1998)

ABSTRACT

The authors consider quasi-stationary planetary waves that are excited by localized midlatitude orographic forcing in a three-dimensional primitive-equation model. The waves propagate toward subtropical regions where the background flow is weak and the waves are therefore likely to break. Potential vorticity fields on isentropic surfaces are used to diagnose wave breaking. Nonlinear pseudomomentum conservation relations are used to quantify the absorption–reflection behavior of the wave-breaking regions. Three different three-dimensional flow configurations are represented: (i) a barotropic flow, (ii) a simple baroclinic flow, and (iii) a more realistic baroclinic flow. In order to allow the propagation of large-scale waves to be studied over extended periods for the baroclinic flows, the authors apply a mechanical damping at low levels to delay the onset of baroclinic instability.

For basic states (i) and (ii) the forcing excites a localized wave train that propagates into the subtropics and, for large enough wave amplitude, gives rise to a reflected wave train propagating along a great circle route into midlatitudes. It is argued that the reflection is analogous to the nonlinear reflection predicted by Rossby wave critical layer theory. Both the directly forced wave train and the reflected wave train are quite barotropic in character and decay due to the damping. However, the low-level damping does not inhibit the reflection. The authors also consider the effect of thermal damping on the absorption–reflection behavior and find that, for realistic wave amplitudes, reflection is not inhibited by thermal damping with a timescale as low as 5 days.

For the third basic state it is found that the small-amplitude response has the character of a longitudinally propagating wave train that slowly decays with distance away from the forcing. The authors argue that part of this decay is due to low-latitude absorption and show that at larger amplitudes the decay is inhibited by nonlinear reflection.

The authors also compare for each basic state absorption–reflection behavior for isolated wave trains and for waves forced in a single longitudinal wavenumber.

## 1. Introduction

Understanding the low-frequency longitudinal variations in the tropospheric circulation remains an important problem. Atmospheric teleconnection patterns have been interpreted for some time as manifestations of large-scale Rossby wave propagation (e.g., Wallace and Gutzler 1981). While recent work (e.g., Branstator 1992) has suggested strong interaction between transient eddies and low-frequency variations, it appears that there is still much to be gained from simple models that treat the low-frequency variations in isolation, for example, based on simple models of Rossby wave propagation (e.g., Branstator 1983; Ambrizzi and Hoskins 1997 and references therein). However, it is clear that models based purely on linear theory must be limited in their usefulness. Observations of the potential vorticity (PV) field (e.g., Hsu et al. 1990; Kiladis and Weickman 1992) show the subtropical upper troposphere to be a region of strong Rossby wave breaking, analogous to the ''surf zone'' in the midlatitude winter stratosphere. Just as in the stratosphere, the tropospheric flow is highly inhomogeneous, with wavelike parts of the flow in close proximity to wave-breaking regions where the flow is highly nonlinear. In order to determine the significance of the simple Rossby wave propagation models, and to improve them where necessary, it is important to understand the interaction between the nonlinear regions and the rest of the flow.

One model problem in which this interaction is particularly clear is the nonlinear Rossby wave critical-layer problem describing the behavior of small-amplitude waves on a basic-state shear flow containing a critical line (a location where the phase speed of the waves

*Corresponding author address:* Dr. Gudrun Magnusdottir, Department of Earth System Science, University of California, Irvine, Irvine, CA 92697-3100.
Email: gudrun@uci.edu

matches the flow speed). Provided that dissipation is sufficiently weak, wave breaking occurs in the neighborhood of the critical line, called the critical layer, even though the waves are small amplitude. The advantage of the critical-layer theory is that it makes precise the interaction between wave-breaking and wave-propagation regions, using the machinery of matched-asymptotic expansions, under the assumption that the wave-breaking region—the critical layer—is thin. The interaction is naturally expressed in terms of whether the critical layer absorbs or reflects the waves outside it. The theory predicts that, when a wave source is switched on, there is initially propagation of the waves toward the location of the critical layer, which appears to act as a wave absorber. As time goes on, the vorticity field is rearranged advectively within the critical layer. This changes the wave field outside with the effect that the critical layer begins to act as a wave reflector. The reflection is manifested as a reduction in the net wave propagation toward the critical layer. One might say that the critical layer acts as a source of waves and that it is the propagation of those waves away from the critical layer that reduces the net propagation toward it. The detailed time evolution of the absorption–reflection behavior may be predicted by numerical solution, or in certain special cases by analytical solution, of the critical-layer equations (see Stewartson 1978; Warn and Warn 1978; Killworth and McIntyre 1985, hereafter KM; Haynes 1989 and references therein).

We might then pose the question, does the tropospheric subtropical wave-breaking region absorb or reflect Rossby waves incident from midlatitudes? Certainly linear wave calculations suggest that the structure of midlatitude Rossby waves depends quite sensitively on this. One might hope to identify the signature of low-latitude Rossby wave reflection in tropospheric teleconnection patterns. It has been difficult to find any robust signature of such reflection. For example, Plumb (1985) calculated wave-activity fluxes from a climatological dataset of 10 Northern Hemispheric winters based on daily NMC (now the National Center for Environmental Prediction) analysis from 1965 to 1975 and found no evidence of poleward propagation out of the subtropics (which might indicate reflection). However, more recently there has been some positive evidence for reflection, for example, in the results of Molteni et al. (1990). Their Fig. 10 shows a composite map of the Pacific–North American pattern that includes not only a wave train extending from the equatorial Pacific, over North America, and equatorward, but also a second wave train emerging from the Caribbean and extending over the North Atlantic and Eurasia. This second wave train might be interpreted as arising from low-latitude reflection of the first. Its amplitude is weak, but Molteni et al. claim that it is statistically significant. Randel and Williamson (1990) computed Plumb's (1985) wave-activity flux for stationary waves in DJF-mean European Centre for Medium-Range Weather Forecasts (ECMWF) analysis for 1980–86. According to their Fig. 18c there is a poleward directed flux at about 170°W, perhaps corresponding to reflection. Yang and Gutowski (1994) used the same diagnostic on a 12-yr DJF-mean dataset of NMC analysis from the years 1978–90. They detected a weak but clearly defined poleward flux of wave activity at longitudes that would be consistent with reflection from a low-latitude wave-breaking region (see their Fig. 4a). As the authors note, the differences between their results and those of Plumb (1985) may be the result of the many changes in the NMC analysis scheme over the period 1965–90. Schubert and Park (1991) computed Plumb's flux from DJF ECMWF winter data from 1981 to 1987. Their Fig. 9b indicates a strong wave-activity flux from low to high latitudes in the central Pacific region. This is apparently due to significant reflection in the vicinity of the equatorward flank of the east Asian jet.

There have also been attempts to identify nonlinear reflection in GCM data. Cook and Held (1992) did not see any evidence of reflection in idealized low-resolution GCM simulations with a zonally symmetric climate and a simple topographic forcing of large-scale waves. Neither did Yang and Gutowski (1994) find evidence of reflection in wave-activity fluxes computed from data generated by two different GCMs, the NCAR and GFDL models (although they had seen such evidence in the fluxes computed from NMC data). All three GCMs considered in these two papers had a horizontal resolution of only R15 and it might well be that this coarse resolution is the reason for the lack of reflection. The hyperdiffusion required for numerical stability at these low resolutions may well be strong enough that the low-latitude flow is more akin to acting as a dissipative critical layer in the nonlinear wave-breaking region. In that case, the nonlinear wave-breaking region would act as a persistent wave absorber. We comment further on this issue in section 7.

Certainly there is theoretical work, outside the small-amplitude restriction of critical layer theory, that gives useful insight into when reflection is to be expected. Killworth and McIntyre (1985) used a nonlinear wave-activity conservation relation to deduce that, under certain restrictions, wave-breaking regions would, if they remained of finite width, act as reflectors in the time average. One of the important limitations on the KM result is that it applies only in a longitudinally averaged sense. Observational studies (e.g., Wallace and Hsu 1983) have shown that tropospheric low-frequency disturbances tend to be longitudinally localized wave trains travelling along great circle routes, rather than being ''monochromatic'' waves with a well-defined longitudinal wave number. As discussed by Brunet and Haynes (1996, hereafter BH), the KM result puts only weak contraints on the absorption–reflection behavior of such wave trains.

Brunet and Haynes (1996) used numerical simulations in a shallow-water model to gain further insight

into this issue. They found clear evidence of low-latitude reflection of a quasi-stationary Rossby wave train forced by an isolated mountain. A previous investigation by Waugh et al. (1994), using contour dynamics, also noted evidence of low-latitude reflection of isolated wave trains.

In order to determine the significance of the above results for the real troposphere, it is natural to extend these investigations to consider fully three-dimensional flows. The results of such an investigation are reported in this paper. Part of the analysis will be based on nonlinear wave-activity diagnostics. These are discussed in section 2. The numerical model is briefly described in section 3. The remainder of the paper describes results from a sequence of numerical experiments, each with a different basic-state flow, and discusses their significance. In each case results for a localized wave forcing, giving rise to a longitudinally localized wave train, and for a monochromatic, wavenumber-3 forcing, are contrasted and the effects of radiative damping on the absorption–reflection behavior are assessed. First, in section 4, the basic state is taken to be an idealized three-dimensional barotropic flow. This is intended to give the closest possible resemblance to the BH case, albeit in a 3D model where the wave forcing is at the surface and waves propagate in the vertical as well as in the horizontal. Sections 5 and 6 consider, respectively, a simple baroclinic flow that includes an upper-tropospheric jet and a flow that is closer to the observed wintertime longitudinal mean. The results are summarized and discussed in section 7.

## 2. Diagnostics

The advantages of using wave-activity fluxes to diagnose wave behavior in numerical simulations and in observations have been demonstrated, for example, by Edmon et al. (1980) and Plumb (1985). For problems in which wave amplitudes are not small, there is a particular advantage in using wave activities for which there is a finite-amplitude conservation relation; that is, there are, in conservative flows, no sources or sinks of wave activity associated with finite-amplitude effects. Wave activities that are conserved at finite amplitude have been constructed in two ways. The first arises from the generalized Lagrangian mean formalism of Andrews and McIntyre (1978). The second exploits the energy–Casimir or momentum–Casimir methods pioneered by Arnol'd to prove stability theorems for Hamiltonian systems. Its usefulness for constructing wave-activity conservation relations was first shown by McIntyre and Shepherd (1987). The second has the great practical advantage over the first that the various wave quantities may usually be expressed in terms of Eulerian variables, without knowledge of particle displacements. Wave-activity diagnostics of the second type have been applied to a range of different flows. See, for example, Scinocca and Peltier (1994) for application to two-dimensional stratified flow over topography, BH for application to Rossby wave propagation in shallow-water models, and Magnusdottir and Haynes (1996) for application to nonlinear baroclinic life cycles.

In this paper we use wave-activity conservation relations for the primitive equations[1] first derived by Haynes (1988). For completeness, we shall write down the relevant expressions again here. Any calculation of wave activity requires the division of flow quantities into basic-state and disturbance parts. If the wave activity is to be conserved at finite amplitude it is important that the basic state be a self-consistent solution of the equations of motion and that it have some symmetry property. We shall use basic states that are independent of longitude; the resulting wave activity is usually referred to as ''angular pseudomomentum,'' or ''pseudomomentum'' for short.

Let $(\cdot)_0$ denote a basic-state variable and $(\cdot)_e$ denote the deviation of that variable from the basic state, such that $(\cdot) = (\cdot)_0 + (\cdot)_e$. The independent variables are the usual spherical coordinates $(\lambda, \phi)$, longitude and latitude, in the horizontal, and potential temperature $\theta$ in the vertical; $a$ is the radius of the earth. The form of the conservation law for pseudomomentum may be written as

$$\frac{\partial A}{\partial t} + \nabla \cdot \mathbf{F} = \frac{\partial A}{\partial t} + \frac{1}{a\cos\phi}\frac{\partial F^{(\lambda)}}{\partial \lambda} + \frac{1}{a\cos\phi}\frac{\partial (F^{(\phi)}\cos\phi)}{\partial \phi} + \frac{\partial F^{(\theta)}}{\partial \theta} = S, \quad (2.1)$$

where the pseudomomentum density $A$ is given by

$$A = -\sigma_e u_e \cos\phi + \sigma \int_0^{P_e} (m_0(P_0 + \tilde{P}, \theta) - m_0(P_0, \theta))\, d\tilde{P}, \quad (2.2)$$

and the components of the flux $\mathbf{F}$ are given by

$$F^{(\lambda)} = uA - \frac{1}{2}\sigma_0(u_e^2 - v_e^2)\cos\phi - \tau(p_e, p_0, \theta)\cos\phi, \quad (2.3a)$$

$$F^{(\phi)} = vA - \sigma_0 v_e u_e \cos\phi, \quad (2.3b)$$

$$F^{(\theta)} = g^{-1}a^{-1}p_e M_{e\lambda}. \quad (2.3c)$$

Here $S$ is given by a rather complicated expression, as shown in Haynes (1988), the negative of the right-hand side of Eq. (3.12a) therein. As stated before, $S$ only involves nonconservative terms. In the above, $(u, v)$ are horizontal components of the velocity, $\sigma = -g^{-1}\,\partial p/\partial\theta$ is the mass per unit volume in isentropic coordinates,

$$P = \left[\frac{2\Omega\sin\phi + \partial v/a\cos\phi\,\partial\lambda - \partial(u\cos\phi)}{a\cos\phi\,\partial\phi]}\right] \Big/ \sigma$$

[1] In the primitive equations the fluid is taken to be hydrostatic and an ideal gas.

is PV, and $M = \Pi\ \theta + gz$ is the Montgomery streamfunction, where $z$ is geometric height, $\Pi = c_p(p/p_s)^\kappa$ the Exner function, and $p_s$ is a reference pressure. The function $m_0(\cdot)$ is defined by

$$m_0(P_0(\phi,\ \theta)) = \int_0^\phi \sigma_0(\tilde{\phi},\ \theta) a\ \cos\tilde{\phi}\ d\tilde{\phi} \qquad (2.4)$$

and is single valued when, for each $\theta$, PV is a monotonic function of latitude. According to (2.4), $m_0$ is the mass in the infinitesmal isentropic layer surrounding $\theta$, measured from the equator to that latitude, $\phi$, where the potential vorticity of the basic state has the value $P_0$. (Recall that the basic state is zonally symmetric.) For ease of interpretation and for comparison with two-dimensional balanced flow, it is easiest to think of $m_0$ as being a measure of position in the latitudinal direction based on the basic-state PV field on each isentropic surface. Then the integral in (2.2) represents a measure of the excursion of fluid particles in the disturbed flow away from the basic state. The function $\tau$ is defined by

$$\tau(p_e,\ p_0, \theta) = g^{-1} \int_0^{p_e} \frac{\kappa\tilde{p}}{(p_0 + \tilde{p})} \Pi(p_0 + \tilde{p}, \theta)\ d\tilde{p}. \qquad (2.5)$$

Note that the sign convention is different from that of Haynes (1988) so that under quasigeostrophic scaling $A$ agrees with the usual definition of Eliassen–Palm wave activity.

For small Rossby number flows it can be shown that the second term in the expression for pseudomomentum density (2.2) dominates the first term. This second term expresses the wave activity arising from PV rearrangement in the flow and is comparable to KM's expression for pseudomomentum density in the case of two-dimensional vortex dynamics. The KM bound on the time-integrated wave-activity flux into the wave-breaking region depends on bounding the wave activity by a function involving the disturbance PV and hence particle displacements. The presence of the first term in (2.2) means that this is not possible for the primitive equations, although for flows that are close to being balanced the expectation is that a bound is likely to hold in practice. This was indeed confirmed by BH for the shallow-water case.

As is well known (e.g., Plumb 1985), and apparent from (2.1), there is substantial indeterminacy in the definition of the pseudomomentum density and flux. For example, we can add a nondivergent part to **F** and (2.1) would still be satisfied. Similarly, we could add parts to both $A$ and **F**, provided that either the time derivative of the part added to $A$ equals the divergence of the part added to **F** or the difference between them involves nonconservative terms only that can be absorbed on the right-hand side. Of course, anything added to the relation must be quadratic in the small-amplitude limit.

Since the components of the flux in (2.3a)–(2.3c) involve unaveraged quadratic functions of wave variables, they will in general be phase dependent. Plumb (1985) derived a locally valid quasigeostrophic wave-activity relation valid for small-amplitude waves on a zonally symmetric basic state and demonstrated that, for stationary waves, the phase dependence of the flux could be removed by adding a correction allowed by the indeterminacy mentioned above. The flows considered here are not quasigeostrophic, but it turns out to be extremely beneficial to apply the same sort of correction as Plumb (1985) to the three-dimensional pseudomomentum flux. Brunet and Haynes (1996) exploited the same method for the two-dimensional case. The method can be extended to the case of waves with nonzero phase speed (Esler 1997), but here we shall concentrate on quasi-stationary waves excited by stationary forcing.

In the three-dimensional case the ''Plumb-corrected'' flux takes the form

$$\hat{F}^{(\lambda)} = F^{(\lambda)} + \frac{\partial}{a\ \partial\phi}\Psi_1 + \frac{\partial}{\partial\theta}\Psi_2, \qquad (2.6a)$$

$$\hat{F}^{(\phi)} = F^{(\phi)} - \frac{\partial}{a\ \cos\phi\ \partial\lambda}\Psi_1, \qquad (2.6b)$$

$$\hat{F}^{(\theta)} = F^{(\theta)} - \frac{\partial}{a\ \cos\phi\ \partial\lambda}\Psi_2, \qquad (2.6c)$$

where

$$(\Psi_1,\ \Psi_2) = \frac{1}{2}(-u_e\psi_e\sigma_0\ \cos\phi,\ g^{-1}p_eM_e\ \cos\phi) \qquad (2.7)$$

and $\psi$ is the streamfunction for the nondivergent part of the horizontal flow.

Later in the paper we show explictly that this correction is indeed effective at removing the phase-dependent structure in the flux pattern.

## 3. Model, forcing, and basic-state flows

The numerical model used in the simulations is the University of Reading, primitive-equation, sigma-coordinate model developed by Hoskins and Simmons (1975). It was run at T42 horizontal resolution and with 15 sigma levels in the vertical; at sigma = 0.967, 0.887, 0.784, 0.674, 0.569, 0.477, 0.400, 0.338, 0.287, 0.241, 0.197, 0.152, 0.106, 0.060, and 0.018. The corresponding level mean temperatures are 283.2, 279.1, 273.3, 266.1, 258.1, 249.8, 241.5, 234.0, 227.2, 220.5, 213.0, 204.3, 195.3, 199.7, and 208.5 K.

The model has $\nabla^6$ hyperdiffusion added to the vorticity, divergence, and temperature tendency equations with a decay rate of 10 day$^{-1}$ for the smallest resolved horizontal scales. The zonally symmetric flow was defined by choosing a height–latitude profile for the zonal velocity and using this as an initial condition. The latitudinally varying part of the initial temperature fields was chosen to be in gradient wind balance with the initial wind fields. The resulting basic states remained statically stable.

Longitudinal asymmetries were forced in the flow by

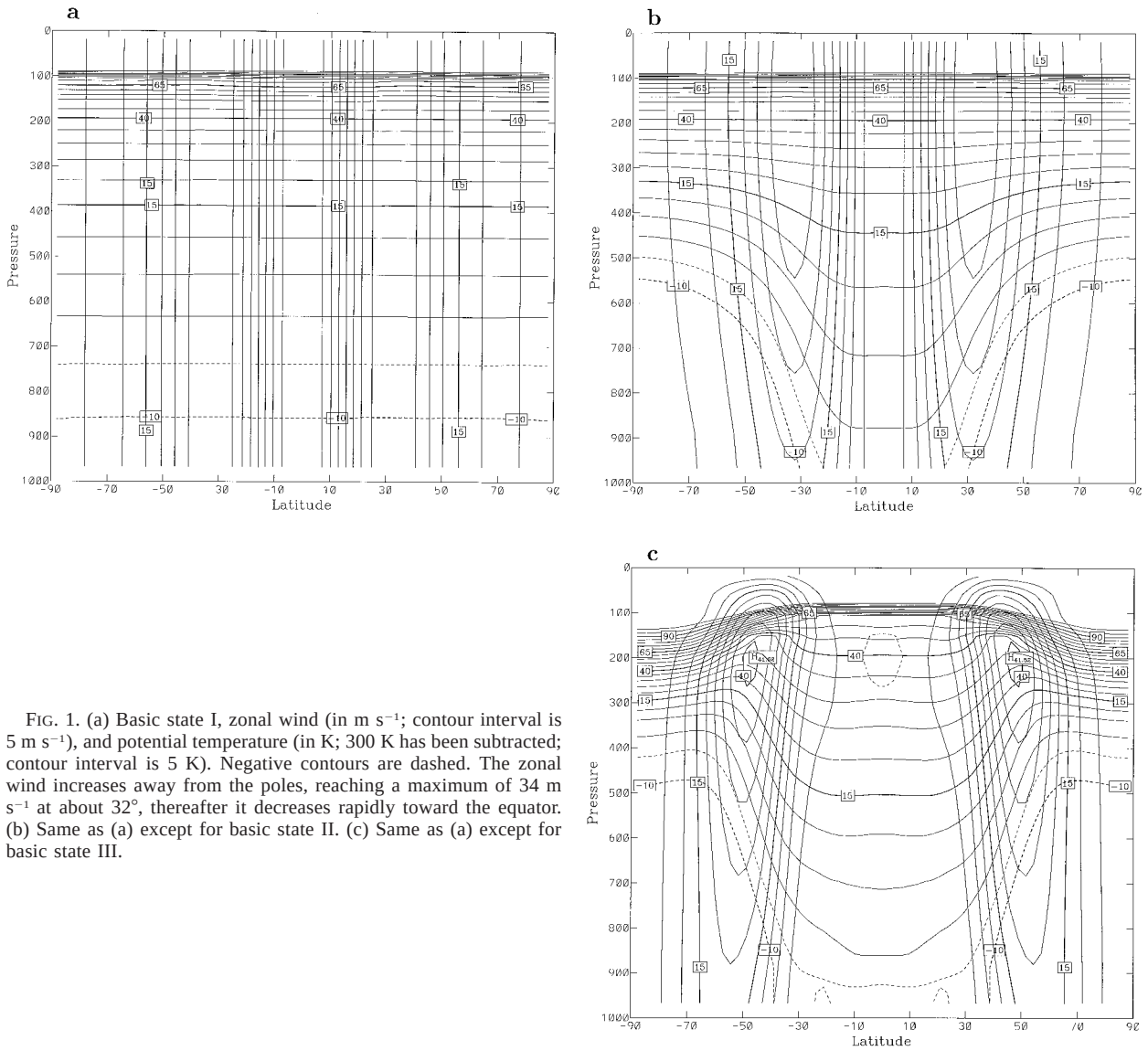


FIG. 1. (a) Basic state I, zonal wind (in m $s^{-1}$; contour interval is 5 m $s^{-1}$), and potential temperature (in K; 300 K has been subtracted; contour interval is 5 K). Negative contours are dashed. The zonal wind increases away from the poles, reaching a maximum of 34 m $s^{-1}$ at about 32°, thereafter it decreases rapidly toward the equator. (b) Same as (a) except for basic state II. (c) Same as (a) except for basic state III.

placing a Gaussian-shaped mountain at 45°N and 180°E, with a half-radius of 1066 km. This is the shape of the forcing originally used by Grose and Hoskins (1979). Additionally, we considered wave-3 forcing, imposing periodicity in the longitudinal direction while keeping the mountain Gaussian in latitude. The height of the mountain was smoothly increased from zero to its steady-state value over the first 4 days of each simulation. A nondimensional forcing amplitude $\delta$ is defined by $\delta = h/h_0$, where $h$ is the maximum height of the mountain and $h_0 = 840$ m. The effectiveness of the forcing also depends, for instance, on the low-level wind speed at the location of the mountain. However, for each set of experiments involving a particular basic-state flow, the nondimensional height is a useful measure of the forcing.

Three different basic-state wind profiles were used. For the first set of experiments, reported in section 4, the latitudinal wind profile at all levels is that of Held (1985). This wind profile, shown in Fig. 1a, is a simple representation of upper-tropospheric flow. It is symmetric about the equator, with a jet of maximum velocity 34 m $s^{-1}$ centered at about 32° and is easterly only equatorward of about 7°. The second profile (shown in Fig. 1b), for which results are reported in section 5, was generated simply by multiplying the first by $\text{sech}^2$(sigma $-$ 0.175). This was designed to introduce the extra realism of vertical shear in as simple a way as possible. However, this second profile has some important differences from observed tropospheric wind profiles. In particular, the resulting basic state has a static stability profile that implies that the tropopause is of approximately the same height at all latitudes.

The third velocity profile (shown in Fig. 1c), for

which results are reported in section 6, is closer to the observed wintertime mean flow. It is closely related to the profile that was used in Magnusdottir and Haynes (1996), as the initial state for the life cycle experiment termed LC1. That profile has been used in a number of other studies of baroclinic life cycles. Here we moderate the LC1 profile to avoid the problems associated with the fact that the latitudinal PV gradient on isentropic surfaces changes signs. Additionally, we extend this profile to both hemispheres by imposing symmetry about the equator. Together with our choice of vertical profile for global mean temperature (which is given above), this wind profile gives a realistic looking tropopause.

For simulations in which the basic-state flow had nonzero vertical shear, it was necessary to inhibit the growth of baroclinic disturbances; otherwise, over 20 days or so, such disturbances grow to swamp the forced planetary response. Frictional drag represented by linear Rayleigh friction was therefore introduced into the lowest levels of the model. A drag coefficient of 5 $day^{-1}$ at the surface, decreasing in the vertical (linearly with sigma) to zero at sigma = 0.7, was sufficient to inhibit baroclinic growth for the duration of the simulations. The drag coefficient at the surface is of the same order of magnitude as the value 3 $day^{-1}$ suggested by Valdes and Hoskins (1988) to mimic a realistic Ekman layer. Held and Suarez (1994) suggest a value of 1 $day^{-1}$ at the surface, decreasing linearly to zero at sigma = 0.7, as a standard value for intercomparison of general circulation models, but we found that this value was not sufficient to inhibit baroclinic instability.

## 4. Basic state I: Barotropic flow

First we wish to establish what aspects of previous results carry over to the three-dimensional case, without bringing the complicating effects of vertical shear into the problem. The basic-state wind is therefore taken to be, at all heights, exactly that used by BH in the shallow-water study. This basic state is depicted in Fig. 1a.

### *a. Isolated forcing in midlatitudes*

We first consider the case when the only damping is the $\nabla^6$ hyperdiffusion. We then consider the case that additionally has some low-level mechanical damping in order to get an indication of its effect. This aids interpretation of results to be described in later sections for simulations where damping is essential to inhibit the growth of baroclinic disturbances.

Figure 2 shows results for the case of small-amplitude isolated forcing, when the topographic forcing has a nondimensional amplitude of 0.1. Figure 2a shows the meridional wind on sigma = 0.287, 18 days into the simulation. Two different wave trains downstream of the topography are clearly visible, one directed eastward and toward low latitudes and another one directed eastward and poleward. We are particularly interested in the wave train directed toward low latitudes and terminating, and apparently being absorbed, where the background flow becomes weak. This field looks much the same 8 days earlier in the simulation, implying that at 10 days something close to a steady state has been achieved. We interpret this behavior as low-latitude critical-layer absorption, consistent with the hypothesis that, for this amplitude of forcing, the small-scale dissipation in the critical layer, associated with the model hyperdiffusion, is sufficient to dominate nonlinearity.

Figure 2b shows the wave-activity density on the 340 K surface at the same time and for the same forcing. The wave-activity density is a quadratic measure of wave amplitude. Considerable wave activity has accumulated in the region of small background winds where the wave train is incident. The corresponding wave-activity flux while applying the Plumb correction [as expressed in (2.6a)–(2.6b)] is shown in Fig. 2c. Most of the flux is directed into the aforementioned region. Again, both fields look much the same both earlier and later in the simulation, indicating that a steady state has been reached where the small-scale dissipation balances the convergence of flux into the region.

To see the effects of applying the Plumb correction to the wave-activity flux, Fig. 2d shows the pseudomomentum flux without this correction [as expressed in (2.3a)–(2.3b)]. Unlike Fig. 2c, this flux shows considerable structure on the scale of the phase of the waves. It is hard to discern the propagation of the waves from the uncorrected flux. The corrected flux in Fig. 2c gives, on the other hand, a clear view of the wave propagation.

If the forcing is increased to an amplitude of 0.5 the low-latitude response is entirely different. Figure 3a shows PV on the 340 K surface at day 18. There is a primary wave-breaking region where the original wave train was incident on the region of small background winds. Additionally, a secondary region of considerable PV rearrangement is evident at low latitudes close to 0° longitude or the Greenwich meridian. (The Greenwich meridian, which is indicated by ''GM'' in all the figures, runs vertically from the center of the plots to their base.) The corresponding wave-activity density and flux are shown in Figs. 3b and 3c, respectively. The wave-activity density reveals a characteristic double maximum structure in each of the two wave-breaking regions corresponding to the concentration of the PV gradient at the northern and southern edges of such regions. The primary region has much more wave activity than the secondary. We argue that the accumulation of wave-activity in the primary region has saturated and the secondary wave-breaking region arises from breaking of the wave train that was reflected from the primary region. Note that no such secondary wave-breaking region was seen in the previous case of small-amplitude forcing. It cannot therefore be explained, for example, by the presence of a second wave train occuring as part of the small-amplitude response. When comparing the

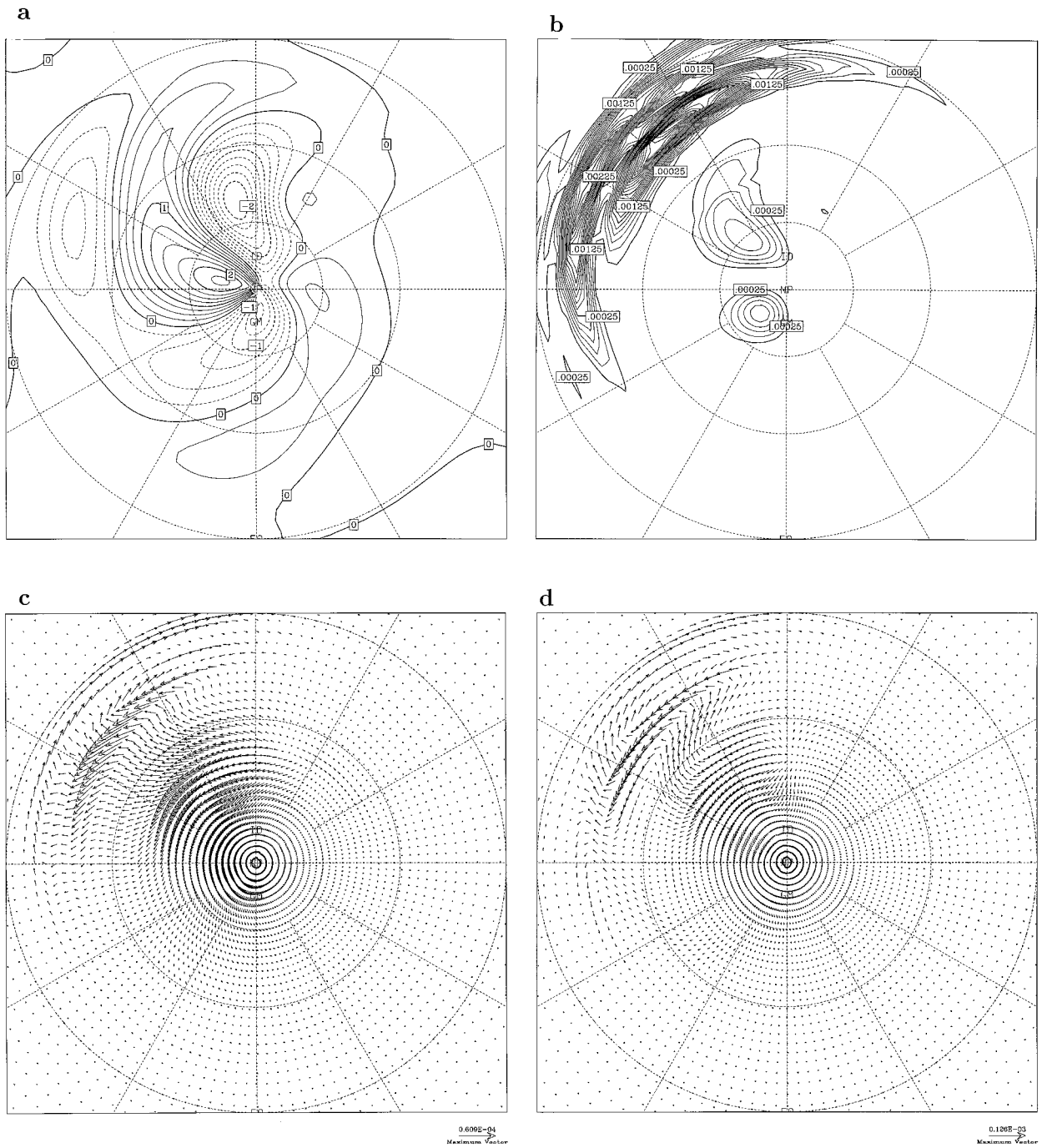


FIG. 2. (a) Meridional wind (in m $s^{-1}$) on sigma = 0.287 for the case of initial barotropic wind field and weak forcing (forcing amplitude 0.1) at day 18. The forcing is located at 45°N, 180°W. The plot is hemispheric. The latitudes depicted are 0°, 30°, and 60°. The meridian running through the center of the figure is 0° longitude, or the Greenwich meridian, in the lower half and 180°, or the dateline, in the upper half of the figure. The contour interval is 0.25 m $s^{-1}$. (b) Pseudomomentum density on the 340 K surface at the same time and for the same initial field and amplitude of forcing. The contour interval is $2.0 \times 10^{-4}$. (c) Pseudomomentum flux for the same case and time on the 340 K surface. (d) Pseudomomentum flux for the same case except now it is without the correction for the phase-dependent part of the flux.

wave-activity density in the two cases or Figs. 3b and 2b, note that the contour interval of the large-amplitude case is greater than the small-amplitude case by the square of the proportionality of the forcing amplitudes.

The reflected wave train emerges from the primary wave-breaking region around 120°W, propagates poleward, and is then refracted back toward low latitudes. It again encounters low background winds and therefore

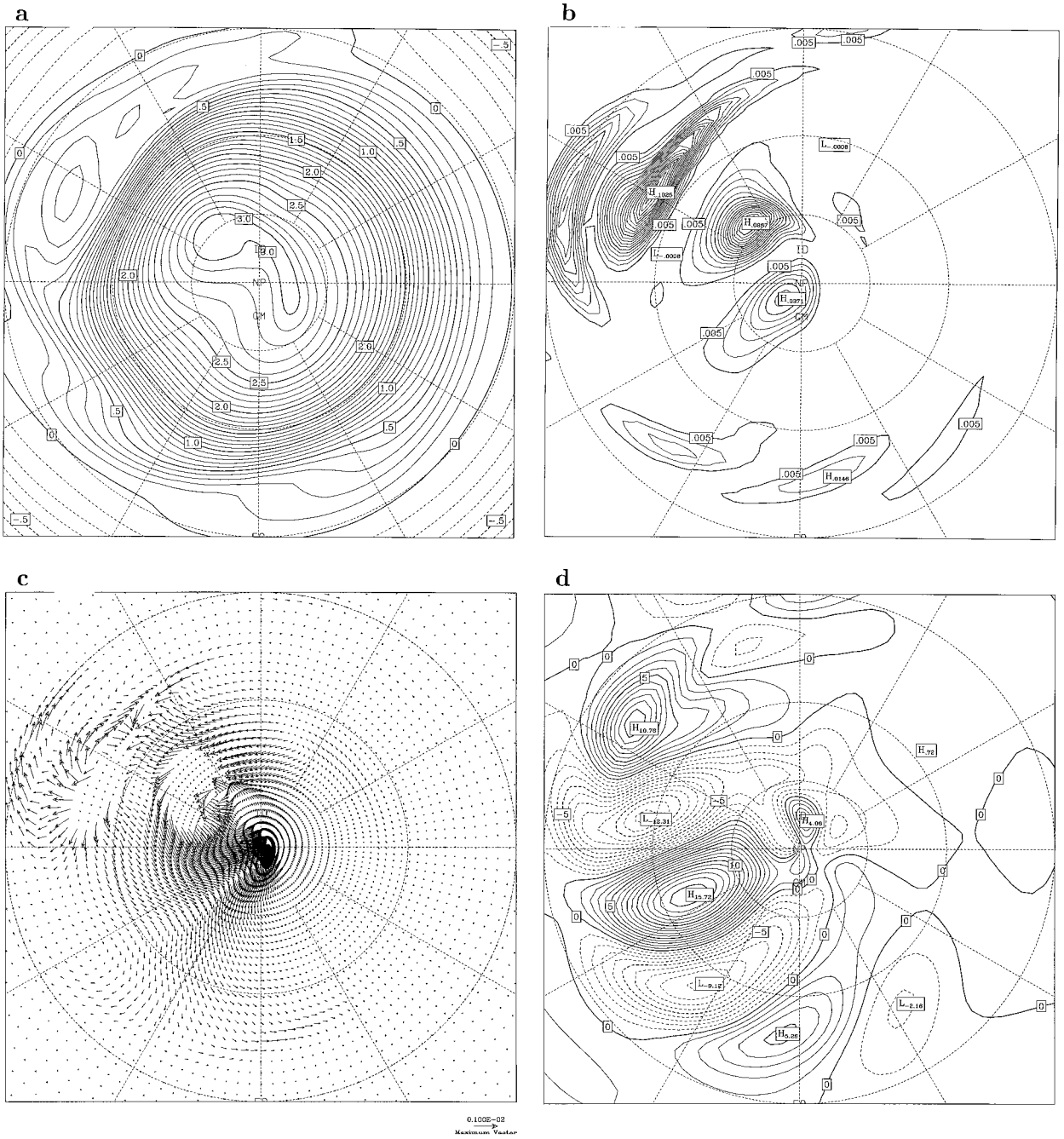


FIG. 3. (a) Potential vorticity on the 340 K surface for the strong-amplitude forcing (0.5) in barotropic initial flow at day 18. Contour interval is 0.1. (b) Pseudomomentum density for the same case on the same surface. Contour interval is $5.0 \times 10^{-3}$. (c) Pseudomomentum flux for the same case on the same surface. For clarity the longest arrows have been removed. Note the flux curving northward out of low latitudes at around 70°W and then curving back equatorward at around 40°–50°W. (d) Difference in meridional wind (normalized by the forcing) between a strong forcing case (amplitude 0.5) and the weak forcing case (amplitude 0.1). On the sigma = 0.287 surface. The initial wind field is barotropic. The contour interval is 1 m $s^{-1}$.

breaks just east of 0° longitude. The wave-activity flux depicted in Fig. 3c certainly appears to be consistent with this description, although at first glance it is dominated by the large fluxes, presumably advective, in the wave-breaking region itself. There is a strong flux into the first wave-breaking region with a return flux evident at longitudes around 80°W, curving back equatorward at around 50°W, and upon reaching low latitudes this flux has largely disappeared.

The reflected wave train may be seen in the difference

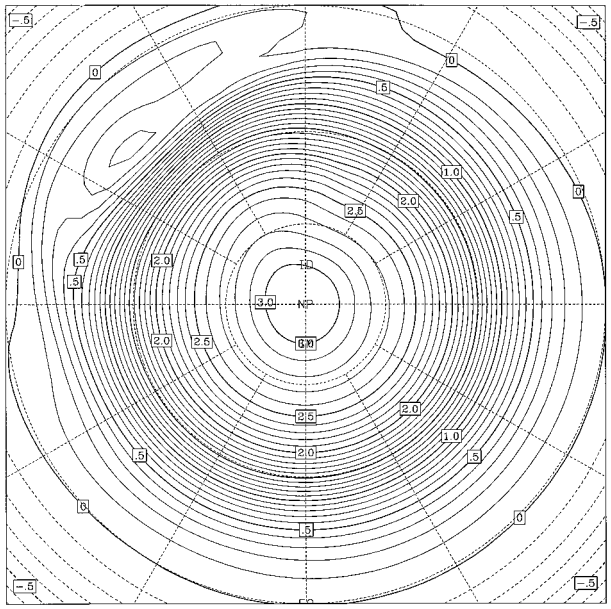

FIG. 4. Same as Fig. 3a except in this case mechanical damping is included. The damping is strongest at the surface ($(0.2\ \text{day})^{-1}$) and goes to zero at sigma = 0.7.

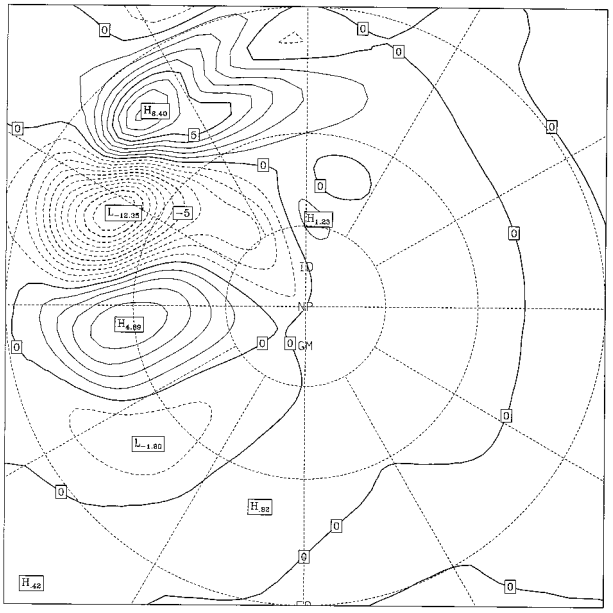

FIG. 5. The difference in meridional wind (normalized by the forcing) between a strong forcing case (amplitude 0.5) and the weak forcing case (amplitude 0.1) on day 18. On the sigma = 0.287 surface. The initial wind field is barotropic. Low-level mechanical damping is included. The contour interval is 1 m $s^{-1}$.

field of meridional velocity between the present case of forcing amplitude = 0.5 and the small-amplitude case of forcing amplitude = 0.1 (where each field has been normalized by the amplitude of the forcing before taking the difference). Figure 3d shows this difference field on the upper-tropospheric sigma level of 0.287 on day 18. The reflected wave train shows up clearly, stretching between the two wave-breaking regions, from the upper left quadrant to the lower left quadrant of the figure. Again, the fact that this wave train shows up only as a difference between linear and nonlinear responses makes it difficult to explain it as any ''split wave train'' linear response.

If low-level mechanical damping is included, the secondary wave-breaking region no longer appears. Figure 4 shows PV at 340 K on the same day of a simulation with the same amplitude forcing as that shown in Fig. 3a, but with low-level damping included. The damping rate is 5 $\text{day}^{-1}$ at sigma = 1, decreasing linearly to zero at sigma = 0.7. For all experiments from here on, this low-level mechanical damping is always included.

There is still wave breaking in low latitudes around 120°W, but the secondary wave-breaking region is no longer visible. (Even reducing the contour interval five times does not reveal the secondary region.) The fields of wave-activity density and wave-activity flux for this same case show a corresponding structure. Even though the second region of wave breaking is no longer identifiable, there is still evidence for a reflected wave train as we shall now show.

Figure 5 shows the difference field of meridional velocity normalized by the amplitude of the forcing between the strong forcing case (0.5) and a case of weak forcing (0.1). A wave train stretching from low latitudes and around 120°W curving poleward and then equatorward again is evident in this figure. Since this wave train is manifested in the difference field it may be regarded as arising from nonlinearities in the flow. Since it is far from the forcing region itself, it is unlikely that it is associated with nonlinearities arising from flow around the mountain. A further piece of evidence that what is seen is indeed reflection out of the wave-breaking region is given in Fig. 6, which shows the equatorward component of the normalized wave-activity flux through 30°N, zonally averaged and summed over 15 equally spaced levels ranging from 310 to 380 K, as a function of time (in days). Results are shown from three experiments with different forcing amplitudes of 0.1 (small amplitude), 0.3 (intermediate amplitude), and 0.5 (strong amplitude). In each case the flux values are normalized by the square of the forcing amplitude. Notice that the small-amplitude run only shows a slight reduction in the average equatorward flux in time. The intermediate-amplitude run shows more reduction in flux and the large-amplitude run shows the greatest overall reduction, with the reduction occurring earlier in the simulation. Similar results are shown by BH for the single-layer case (their Figs. 5 and 6). This result is consistent with predictions of nonlinear critical-layer theory, which are that the larger the amplitude of the forcing, the shorter the time necessary to reach a reflecting state. For the small-amplitude case there is the possibility that there will never be a substantial reduction in the flux and that a quasi steady state is achieved,

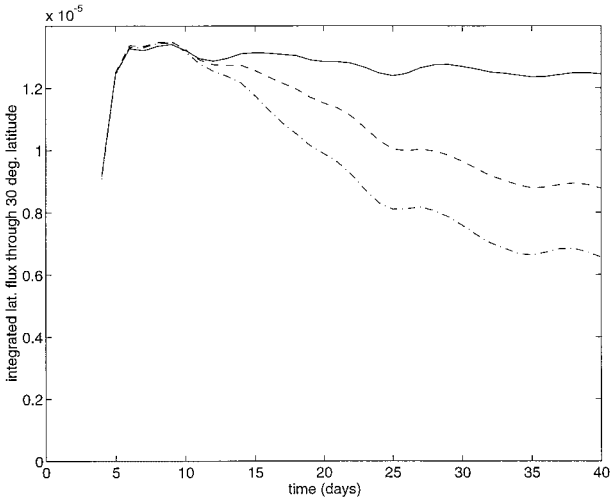


FIG. 6. Barotropic initial winds; mechanical damping is applied at low levels. The zonally averaged and vertically integrated (from 310 to 380 K) normalized equatorward pseudomomentum flux through 30°N as a function of time. Full line represents the small-amplitude case with a forcing amplitude of 0.1, dashed line has a forcing amplitude of 0.3, and dash-dotted line has a forcing amplitude 0.5.

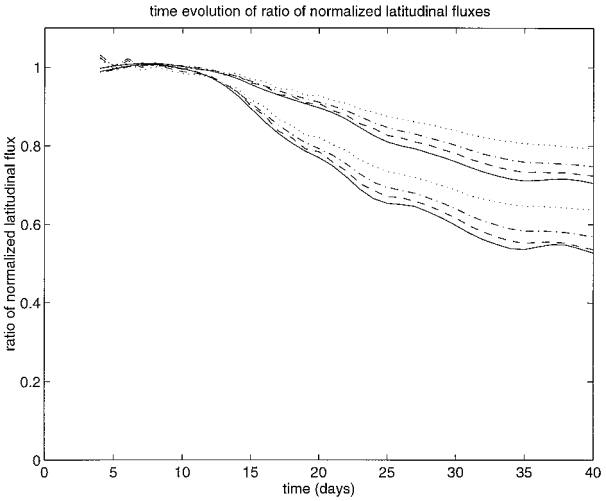


FIG. 7. Barotropic basic state; mechanical damping is applied at low levels. Time evolution of the ratio of the integrated equatorward normalized pseudomomentum flux (for forcing amplitudes 0.3 and 0.5) and the integrated normalized flux for the small-amplitude forcing (0.1), with and without thermal damping. The following cases are plotted: without thermal damping (full curves), with a thermal damping timescale of 20 days (dashed curves), with a thermal damping timescale of 10 days (dashed-dotted), and with a thermal damping timescale of 5 days (dotted).

with low-latitude dissipation of wave activity (primarily due to the model hyperdiffusion) balancing the flux into low latitudes.

### *b. Effects of thermal damping*

In addition to the low-level mechanical damping, we included Newtonian cooling in these experiments to account for radiative damping. Three timescales of Newtonian cooling were considered: 5, 10, and 20 days. The effect of this damping was to reduce amplitudes of the various features in the response (the more so the stronger the damping), but the general pattern remained the same.

Figure 7 highlights the differences of the evolution with and without thermal damping by showing the time evolution of the ratio between the normalized wave-activity flux for each of the larger forcing amplitudes and the normalized wave-activity flux for the small forcing amplitude. A decrease in the ratio implies some reflection (relative to the small-amplitude case). Thus Fig. 6 implies that for the case with no thermal damping, this ratio will decrease from an initial value of one, and that for the largest forcing amplitude (0.5) the decrease will be more rapid than for the intermediate forcing amplitude (0.3). Results are shown in Fig. 7 for thermal damping on timescales of 5, 10, and 20 days, as well as for no thermal damping. It is clear that for both forcing amplitudes the effect of thermal damping is to inhibit reflection, with greater inhibition as the strength of the damping is increased. However, in none of the cases shown is the damping substantially inhibited. This is not unexpected from critical-layer theory, which predicts that substantial reflection will occur when the critical layer turnover time is less than the damping time (e.g., Haynes and McIntyre 1987). Here the turnover time appears, from PV fields, to be less than 5 days. Note that a thermal damping time of 5 days implies a damping time for PV that is somewhat larger, particularly if the associated dynamical structure is deep, as is the case here (e.g., Haynes and Ward 1993).

### *c. Longitudinally periodic forcing*

It is of some interest to consider the effects of a forcing that is periodic in longitude since the KM bound should be more relevant in that case (at least for flows that are close to being balanced). We therefore consider forcing that has a wave-3 structure in longitude, but the same latitudinal profile. Figure 8 shows the equatorward component of the normalized wave-activity flux zonally averaged and summed over 15 equally spaced levels ranging from 310 to 380 K, as a function of time, again for a case where mechanical damping is applied at low levels. The forcing amplitudes were the same as before, that is, 0.1, 0.3, and 0.5. No thermal damping was included. Comparing this figure to Fig. 6 we see that in this case of periodic forcing, where the wave-breaking region fills the whole domain in the longitudinal direction, the reduction in flux is more pronounced. By the end of the simulation for the strong-amplitude forcing case the integrated flux is less than 30% of its maximum value. This is consistent with the single-layer results of BH, who found an even stronger reduction in flux, which again is consistent with the fact that here we include low-level mechanical damping. This certainly reinforces

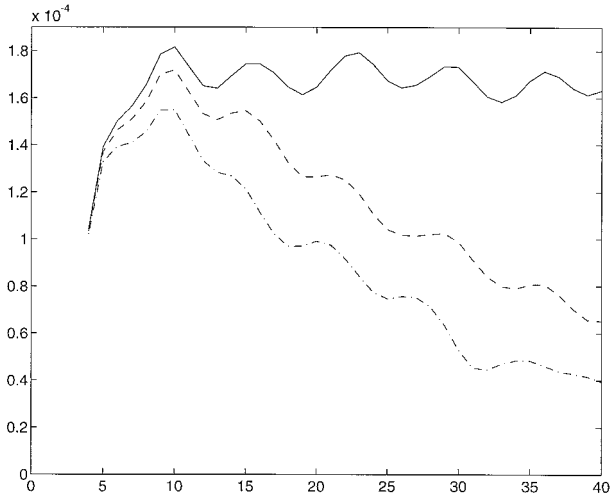


FIG. 8. Same as Fig. 6, except in this case the forcing has a wave-3 structure in longitude.

the general validity of the KM bound, even for primitive-equation simulations, which of course are far different from the two-dimensional vortex dynamics conditions for which the KM result holds.

## 5. Basic state II: Simple baroclinic flow

We now consider the effect of including vertical shear in the basic flow. The velocity profile of the barotropic case described in section 4 was multiplied by the function $\text{sech}^2(\text{sigma} - 0.175)$, putting the jet maximum at sigma = 0.175 in the vertical. This basic state is depicted in Fig. 1b. Note that since now the low-level wind speed is different from the previous, barotropic case, forcing amplitudes are not directly comparable.

### *a. Isolated forcing in midlatitudes*

When a small-amplitude forcing is applied, the response is similar to the case considered in section 4 (Fig. 2). The equatorward wave train terminates at low latitudes around 120°W and a steady state appears to be set up relatively early in the simulation. The wave train is quite barotropic in character (e.g., as revealed by meridional wind at different levels). The fields of PV, wave-activity density, and wave-activity flux are all similar to the linear forcing barotropic case and are not shown here.

Figures 9a and 9b show the fields of PV and wave-activity density on day 16 for a case where the forcing amplitude has been increased ninefold (to 0.9) to give a nonlinear response. Wave breaking has taken place at low latitudes and there has been considerable buildup of wave activity in the wave-breaking region. Figure 9c shows the day 16 difference in wave-activity flux (normalized by the forcing amplitude squared) between the strong amplitude case of 0.9 and the weak-amplitude case of 0.1. Clearly there is a net flux out of the wave-breaking region and into midlatitudes.

We also considered other diagnostic fields and other forcing amplitudes. Figure 10 shows the difference in meridional wind (normalized by the forcing amplitude) between two different nonlinear amplitudes, those of 0.9 and 0.6, and the linear case of amplitude 0.1. The 0.9–0.1 meridional wind difference field on day 14 is shown in Fig. 10a. It looks almost the same as Fig. 10b showing the 0.6–0.1 meridional wind difference field 5 days later, or on day 19. Both fields display a wave train from the low-latitude wave-breaking region that curves eastward and first poleward and then back toward low latitudes. The time lag between the two cases is entirely consistent with the time delay that is predicted by critical-layer theory for the critical layer to become reflecting if the forcing amplitude is reduced by a third.

In Fig. 11 the vertically integrated, zonally averaged equatorward wave-activity flux through 30°N is depicted for four different forcing amplitudes ranging from the linear case of 0.1 to the strongest case of 0.9, with intermediate values of 0.3 and 0.6. In each case the flux is normalized by the forcing amplitude squared. As before, the reduction in flux occurs the earliest and is the most pronounced for the strongest amplitude forcing, with clear evidence of reduction in flux for the other nonlinear case of amplitude 0.6. Even the case with amplitude of 0.3 shows some reduction in flux at longer times.

### *b. Effects of thermal damping*

As in section 4, Newtonian cooling was added, with a timescale ranging from 5 to 20 days, and, as was found there for the barotropic case, the response was damped without changing the general characteristics of the fields in any substantial way. The effects of thermal damping on the absorption–reflection behavior are displayed in Fig. 12 as in Fig. 7, by the ratios of normalized wave activity fluxes. Again, as in the barotropic case, it may be seen that the nonlinear reflection is inhibited by the thermal damping. Comparison of Figs. 7 and 12 suggest that the inhibition may be slightly stronger in the baroclinic case, perhaps because the effects of thermal damping are stronger because the structures in the wave-breaking region are tilted due to the vertical shear in the background flow. (This possibility was suggested to us by Isaac Held.)

### *c. Longitudinally periodic forcing*

With a forcing that is periodic in longitude, the wave-breaking region is of finite longitudinal extent, and the KM bound on how much wave activity can be absorbed is more applicable. Figure 13 shows the zonally averaged and vertically integrated normalized equatorward wave-activity flux through 35°N as a function of time for a forcing that has a wave-3 structure in longitude.

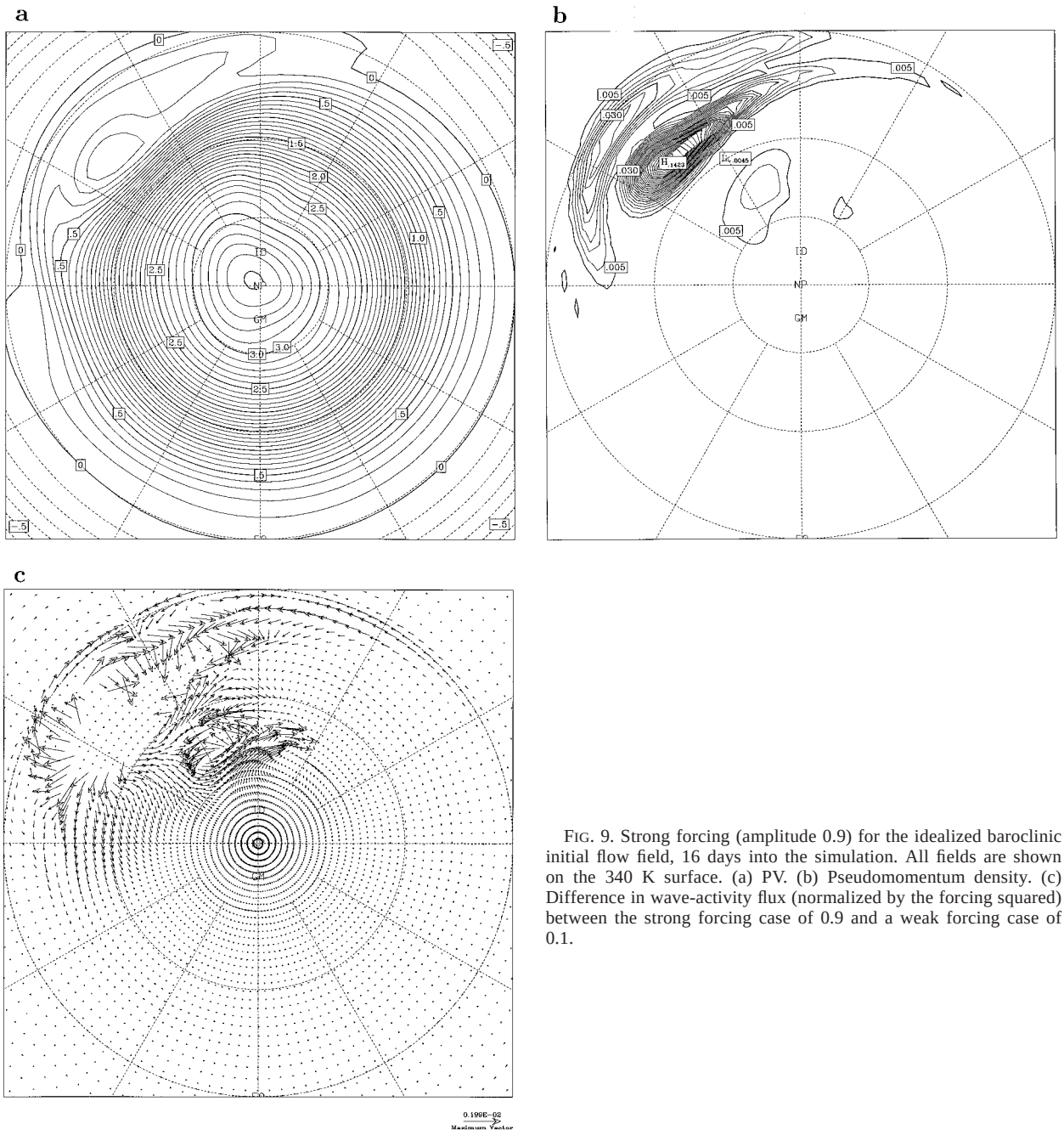


FIG. 9. Strong forcing (amplitude 0.9) for the idealized baroclinic initial flow field, 16 days into the simulation. All fields are shown on the 340 K surface. (a) PV. (b) Pseudomomentum density. (c) Difference in wave-activity flux (normalized by the forcing squared) between the strong forcing case of 0.9 and a weak forcing case of 0.1.

Figure 13 should be compared to Fig. 11, showing the corresponding plot for the isolated forcing cases. For each of the forcing amplitudes leading to nonlinear behavior, the reduction in flux is more pronounced for the wave-3 forcing.

## 6. Basic state III: More realistic baroclinic flow

Here we leave the Held (1985) horizontal wind profile used by BH and consider a basic state that is closer to the observed wintertime mean flow. This basic state is depicted in Fig. 1c. The jet maximum of 41 m $s^{-1}$ is located at 200 hPa and 45° latitude. Symmetry is imposed across the equator. The zero wind line slopes in the vertical, from approximately 17° in the upper troposphere to about 37° at the surface. The tropopause of this basic state slopes upward from high latitudes to the equator. The field of PV on isentropic surfaces in the upper troposphere is much steeper in this case, having very strong gradients in midlatitudes. There is a slight

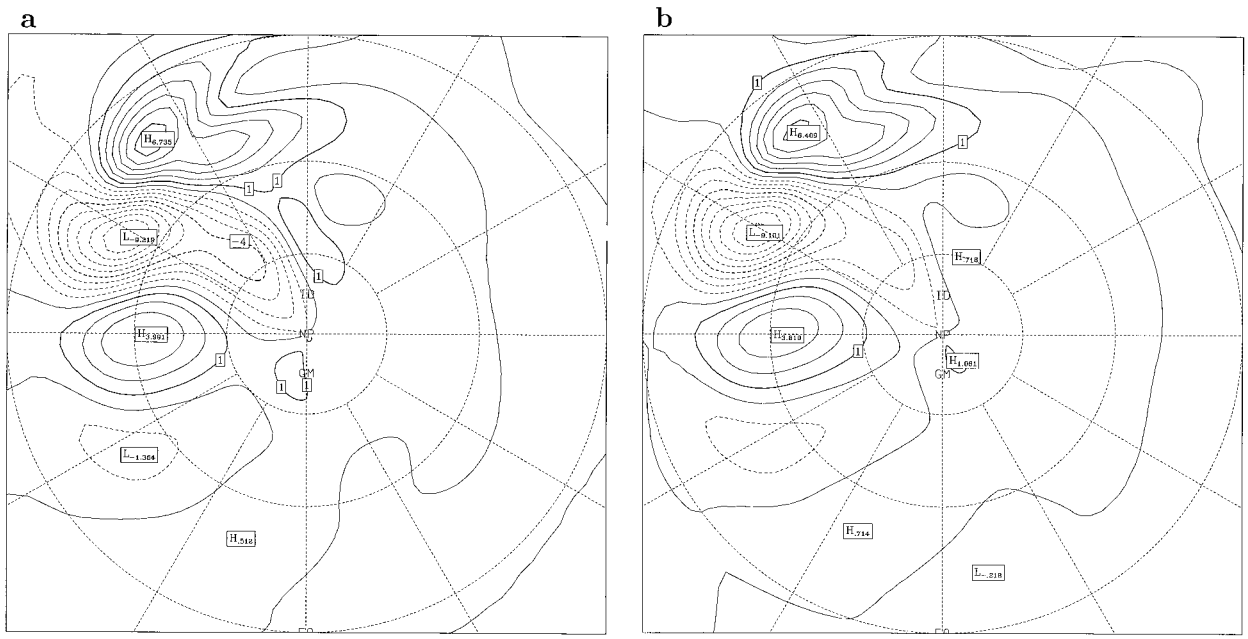


FIG. 10. Initial flow field has an idealized baroclinic jet. Both fields are depicted on sigma = 0.287. (a) Difference in meridional wind (normalized by the forcing) on day 14 between a strong forcing case (amplitude 0.9) and the weak forcing case (amplitude 0.1). The contour interval is 1 m $s^{-1}$. (b) The meridional wind difference field is between a less strong amplitude forcing (amplitude 0.6) and the weak forcing case (amplitude 0.1) on day 19. Same contour interval as in (a).

reversal of PV gradient at high latitudes. This makes results in terms of wave-activity diagnostics unreliable at high latitudes (see Magnusdottir and Haynes 1996 for a detailed discussion of this issue). Since the aim here is to examine wave propagation and breaking at mid- to lower latitudes, we did not attempt any further manipulation of this state.

### *a. Isolated forcing in midlatitudes*

Unlike the previous two cases, here the wave activity tends to be more localized in the vertical at the latitude of wave breaking, attaining maximum values at the 340–345 K level. In this basic state there is also more confinement of wave activity to midlatitudes. This may in part be due to the very small (or even slightly negative)

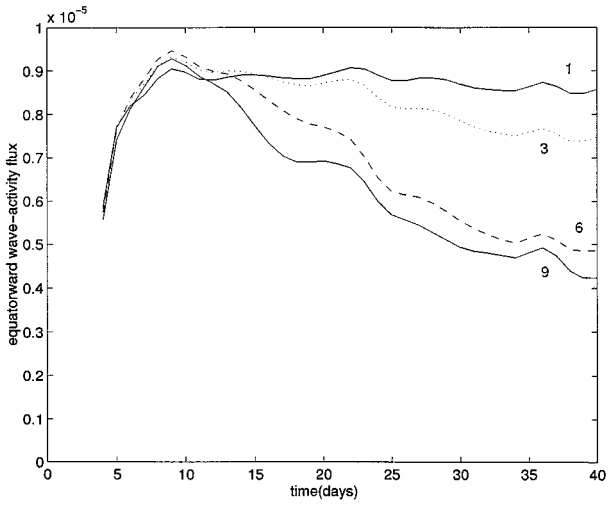


Fig. 11. Same as Fig. 6 except this is for the idealized baroclinic initial state and the four forcing amplitudes are 0.1 (full line), 0.3 (dotted), 0.6 (dashed), and 0.9 (full line).

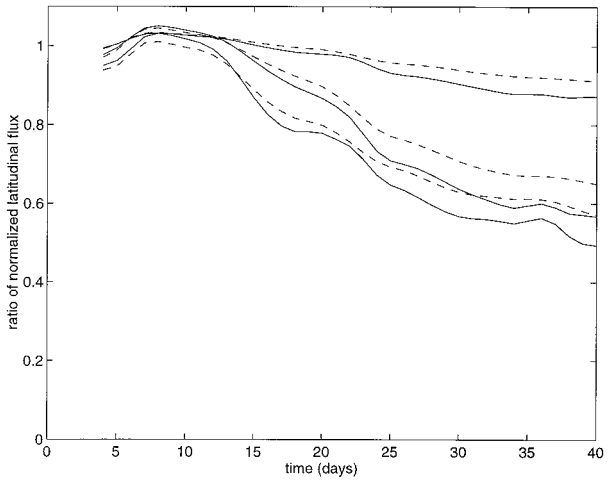


FIG. 12. Same as Fig. 7 except here the idealized baroclinic basic state is depicted and results are only shown for the cases without thermal damping (full curves) and with thermal damping of timescale 10 days (dashed curves). The three forcing amplitudes are 0.9, 0.6, and 0.3.

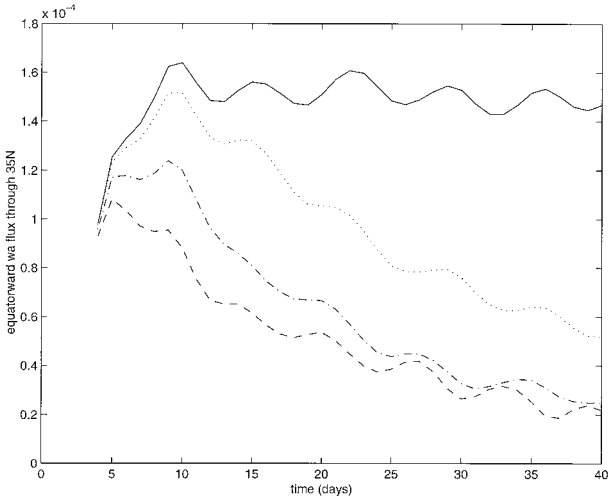


FIG. 13. Same as Fig. 11 except for wave-3 (in longitude) forcing; the equatorward flux is through 35°N.

basic-state PV gradient at high latitudes, blocking poleward propagation, and it may partly be due to the strength of the midlatitude westerlies and the very strong PV gradient in midlatitudes.

First, let us consider results for a small-amplitude case, with nondimensional amplitude of 0.1. Figure 14a shows the upper-level meridional wind, 26 days into the simulation. (Steady state is already reached by day 10.) In both previous basic states, two wave trains were excited by the topography, a poleward propagating one as well as an equatorward propagating one, terminating at low latitudes. Now, only one wave train gets excited. This wave train propagates more or less zonally, decaying slowly with distance away from the forcing. This is consistent with the linear study by Branstator (1983) where similar behavior was found. One mechanism leading to the decay of the wave train is the surface friction. However, this cannot be the only relevant mechanism, since one would expect it to act with equal effect

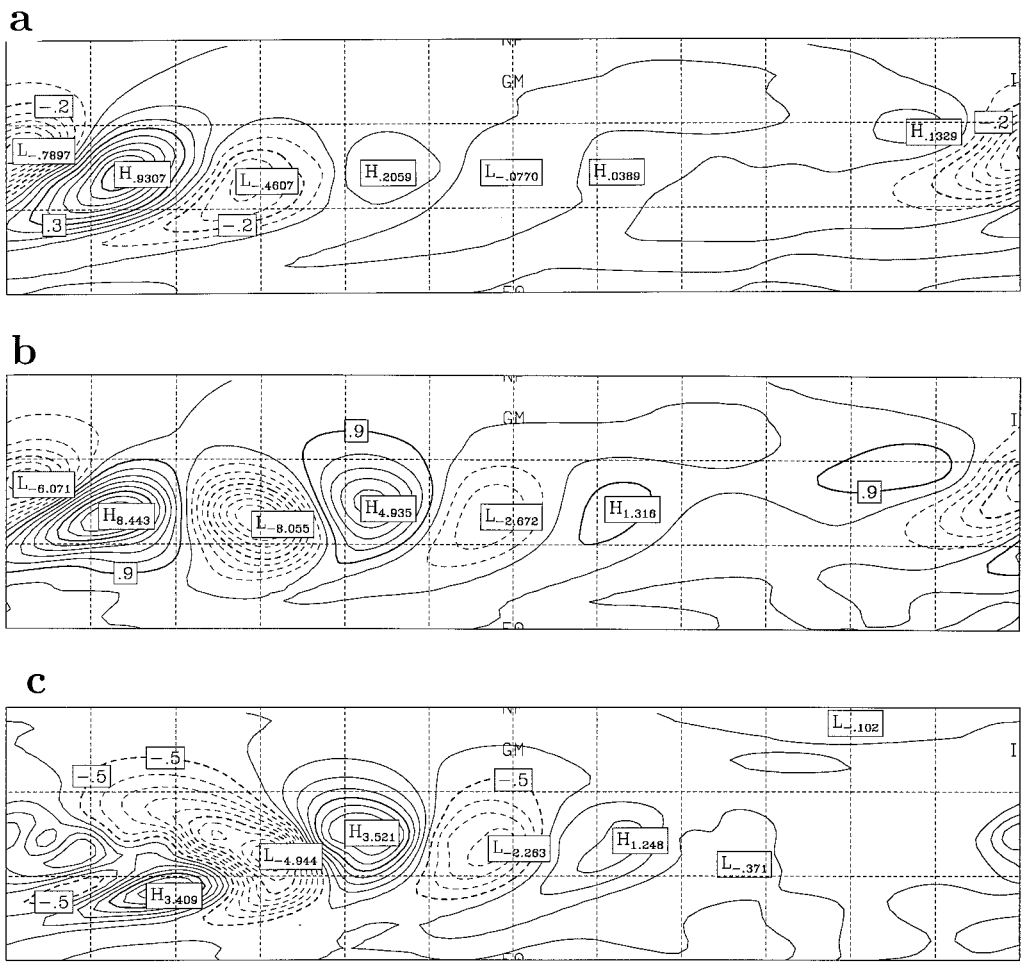


FIG. 14. Basic state III, the more realistic baroclinic state. Mercator projection of the Northern Hemisphere. (a) The meridional wind on sigma = 0.1968 for the case of weak forcing of amplitude 0.1, 26 days into the simulation. The contour interval is 0.1 m $s^{-1}$. (b) Same as (a) except for the strong-amplitude case of 0.9. The contour interval is 0.9 m $s^{-1}$. (c) The difference between the normalized meridional velocity on day 26 for the 0.9 amplitude case [depicted in (b)] and the 0.1 amplitude case [depicted in (a)]. The contour interval is 0.5 m $s^{-1}$.

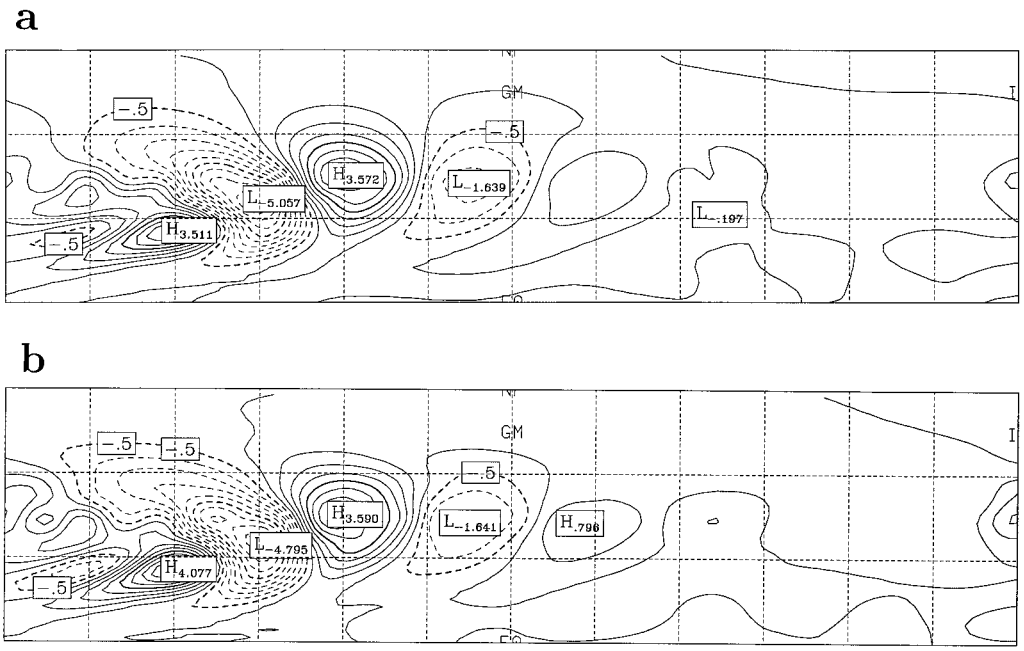


FIG. 15. Basic state III. (a) Same as Fig. 14c except for the 0.6 amplitude case. (b) Same as Fig. 14c except 6 days earlier, on day 20.

at larger amplitude and, as will be shown below, the decay is amplitude dependent. The second mechanism is low-latitude absorption. The basic state in this case appears to confine wave activity to midlatitudes, but the confinement is apparently not perfect and some wave activity is leaking out to be absorbed at low latitudes.

When the forcing amplitude is increased ninefold to 0.9, the wave train reaches farther before decaying, as illustrated in Fig. 14b, which shows the meridional wind on the same vertical level as before and on day 26. Notice that both the contour interval and the forcing in Fig. 14b are nine times what their values are in Fig. 14a. The low-level friction cannot be acting any differently in this case (with larger-amplitude forcing) from the previous case. The difference between the two cases must be the result of differences in the nonlinear absorption–reflection behavior at low latitudes. In the larger-amplitude case the low-latitude region acts to reflect some of the (mostly) zonally propagating wave train.

Figure 14c shows the difference in meridional velocity between the large-amplitude case shown in Fig. 14b and the small-amplitude case in Fig. 14a, after normalizing each one with the amplitude of the forcing. The difference field clearly shows a wave train stretching from low latitudes and about 120°W, and this wave train is quite similar to reflected wave trains seen in the earlier, more idealized simulations.

When the forcing amplitude is decreased slightly to 0.6, which still leads to nonlinear behavior, the nonlinear behavior takes longer to get established. Figure 15a shows the day 26 normalized difference field of meridional velocity for this case and the linear case of forcing amplitude 0.1. This figure should be compared to Fig. 14c, showing the same field and at the same time, but for forcing amplitude 0.9. The wave train does not reach as far in Fig. 15a as in Fig. 14c. If instead of Fig. 14c, we look at the same field generated from the same simulation of forcing amplitude 0.9, 6 days earlier, or on day 20 shown in Fig. 15b, the wave train looks almost the same as in Fig. 15a, for forcing amplitude 0.6 on day 26.

Other forcing amplitudes were also considered and they support the conclusion that given enough forcing, planetary waves will be reflected out of the low-latitude wave-breaking region. The greater the forcing, the earlier the wave-breaking region reaches a reflecting state. Figure 16 shows the zonally averaged and vertically integrated equatorward wave-activity flux through 35°N as a function of time for five different values of forcing. Forcing amplitudes 0.3 and 0.1 show linear behavior with no evidence of the reduction in flux that is associated with nonlinear reflection. Forcing amplitudes 0.6, 0.9, and 1.2 all show the reduction in flux and the time delay when the forcing is reduced that is consistent with previous results.

### *b. Effects of thermal damping*

Two values of thermal damping were considered, with 20- and 10-day timescales. Results are shown in Fig. 17, which corresponds to Figs. 7 and 12, in that ratios of normalized fluxes in large-amplitude cases to normalized flux in a reference small-amplitude case are shown. In this case the amplitudes are 0.6, 0.9, and 1.2,

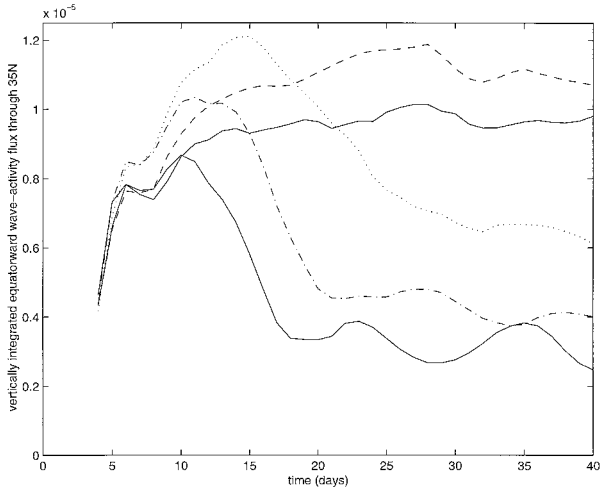


FIG. 16. Same as Fig. 6 except this is for the more realistic baroclinic initial state (basic state III); the five forcing amplitudes are 0.1 (full curve), 0.3 (dashed), 0.6 (dotted), 0.9 (dashed-dotted), and 1.2 (full curve)

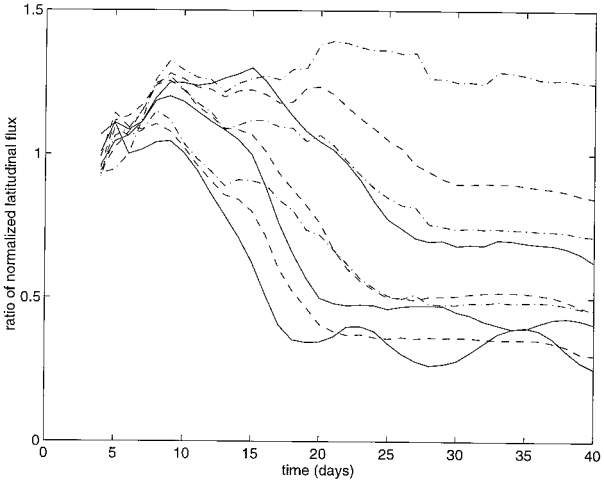


FIG. 17. Same as Fig. 7 except for basic state III. For cases without thermal damping (full curves) and cases with damping timescale of 20 days (dashed curves), and damping timescale of 10 days (dashed-dotted). The amplitudes of forcing plotted here are 0.6, 0.9, and 1.2.

and the reference small amplitude is 0.1. Results for no thermal damping are also shown for comparison purposes. Again, it is clear that increasing the strength of the thermal damping tends to inhibit reflection. Comparing with Fig. 12, which shows results only for no thermal damping and 10-day thermal damping, it appears that the inhibition of the reflection by the damping is greater in the case considered here. Note that at amplitude 0.6, for example, there is almost complete inhibition of the reflection with 10-day thermal damping. With amplitude 0.9 and 10-day thermal damping there is substantial inhibition of reflection, in the sense that the reduction in latitudinal flux from its maximum value is only about 60% of that in the case with no damping.

This stronger effect of damping may, consistent with the argument in section 5b, be due to smaller vertical scales, and hence relatively stronger effects of thermal damping, in the wave-breaking region. This might be expected from the fact that vertical shears in that region are larger for this basic state than they were for that studied in section 5. Nonetheless, it is important to note that even with 10-day damping there is still strong reflection with amplitude 1.2, and the disturbance amplitudes resulting in this case do not seem out of line with those observed in the real atmosphere.

### *c. Longitudinally periodic forcing*

When the flow is forced with topography that has a wave-3 shape in longitude, rather than isolated topography, the response is stronger for a given forcing amplitude. Moreover, the wave-breaking region fills a greater range of longitudes, thus allowing more complete reflection. This is evident in Fig. 18, which is the equivalent of Fig. 16 for the isolated forcing case, depicting the total equatorward flux through 35°N as a function of time. Not only does the reflection occur earlier in the simulation for the same forcing amplitude, it is also more complete, oscillating around an equilibrium value of close to zero for forcing amplitude of 0.9.

## 7. Concluding remarks

We have shown in three-dimensional numerical simulations of increasing complexity that quasi-stationary wave trains propagating to low-latitude regions of low background wind speed may indeed be reflected back to midlatitudes, provided that the forcing is large enough. The results of this study therefore leave open the possibility that reflection of tropospheric wave trains from low latitudes may occur in the real atmosphere.

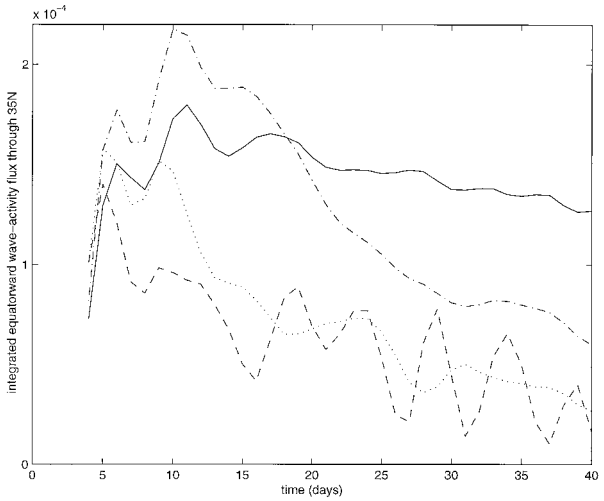


FIG. 18. Same as Fig. 16 except for wave-3 (in longitude) forcing, for the four forcing amplitudes 0.1, 0.3, 0.6, and 0.9.

Evidence from observational data for reflection of tropospheric wave trains from low latitudes is still somewhat equivocal. However, as noted in the introduction, recent studies such as those of Molteni et al (1990), Randel and Williamson (1990), Yang and Gutowski (1994), and Schubert and Park (1991) do give some indications of reflection. It would be interesting to analyze their results more carefully to focus on this issue and to try to understand why reflection was not seen in earlier work such as that of Plumb (1985).

The fact that planetary wave reflection has not been detected in GCM simulations may be due to inadequate resolution. The GCM studies cited in the introduction all had horizontal resolution of R15. Brunet and Haynes (1996) found in their single-layer simulations, in a similar regime of wave amplitudes, that while reflection was observed at T31 horizontal resolution, it was not observed at T21 (which is arguably slightly finer resolution than R15 in the subtropics). To examine this issue in more detail, we ran experiments at lower resolution and therefore necessarily with greater diffusion of the smallest resolved horizontal scales. For basic state III, discussed in section 6, we made runs at T21 and T31 as well as at T42, for which results were presented before. Throughout this paper, for experiments at T42 horizontal resolution, we use $\nabla^6$ diffusion of the smallest horizontal scales with a decay rate of 10 day$^{-1}$. For T31 horizontal resolution, we use $\nabla^6$ diffusion with a decay rate of smallest horizontal scales of 5 day$^{-1}$. For T21 horizontal resolution, we use $\nabla^6$ diffusion with a decay rate of smallest horizontal scales of 4 day$^{-1}$.

Some relevant results are presented in Fig. 19a, which shows the time evolution of the integrated and suitably normalized, equatorward wave-activity flux through 35°N, for three different amplitudes of forcing and for the three resolutions: T42, T31, and T21. The dotted curves represent the smallest forcing amplitude of 0.5. In this case there is a clear reduction in flux for the T42 run, but the T31 run does not show a clear sign of reflection. As the amplitude is increased to 0.75 (dashed-dotted curves), the run at T31 also shows evidence of reflection; however, the T21 run does not show any reduction in flux in time. In fact, even in the most strongly forced case of amplitude 1.0 (dashed curves), the T21 run does not show the reduction in flux indicative of nonlinear reflection. We conclude that at the horizontal resolution of T21, the diffusion that is required for numerical stability makes the low-latitude region act more like a persistent wave absorber than a wave reflector.

To ensure that the behavior that we have just described is indeed the result of increased dissipation at the lower resolution, and not a result of the change in resolution itself, we ran a few experiments at T42 horizontal resolution but with dissipation corresponding to the dissipation needed for numerical stability at T21. In these modified T42 experiments, each wavenumber was damped as if these were experiments run at T21. Some pertinent results are shown in Fig. 19b, which shows

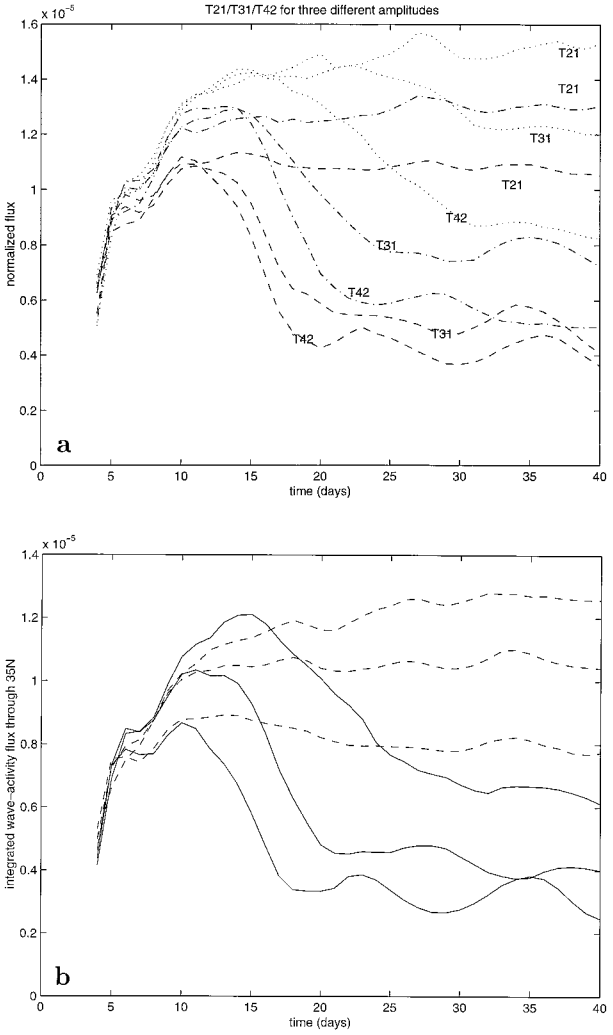


FIG. 19. (a) Same as Fig. 16 except only for three amplitudes of forcing, 0.5 (dotted), 0.75 (dashed-dotted), and 1.0 (dashed), but for three horizontal resolutions: T42, T31, and T21. (b) Same as Fig. 16 except only for the three largest forcing amplitudes or those of 1.2, 0.9, and 0.6 (all solid). The dashed curves represent the same amplitude forcing, but now the T42 experiments are run with the same dissipation as is required for numerical stability in T21 runs.

the time evolution of the integrated equatorward wave-activity flux. Three of the curves in the figure were previously shown in Fig. 16 but are repeated here for comparison. These are the standard T42 experiments that were discussed in section 6a. The three dashed curves show corresponding results obtained when running at T42 but with dissipation corresponding to T21. Note that for the cases with dissipation corresponding to T21 there is no evidence of reflection.

The work reported in this paper is a natural extension of that based on single-layer models reported by BH and Waugh et al. (1994). It seems worthwhile to continue this line of investigation to consider the effect on low-latitude reflection of further dynamical ingredients that have been omitted so far, but which are present in

the real atmosphere. A first ingredient, which would probably be the simplest to investigate, is longitudinal asymmetries, in particular longitudinally localized regions of westerlies, in the Tropics. Webster and Holton (1982) suggested that such westerlies, which are observed in the eastern Pacific and Atlantic, might act as ''ducts'' allowing cross-equatorial wave propagation. Hoskins and Ambrizzi (1993) suggest, on the basis of a linear study, that any cross-equatorial propagation is likely to be weak. In the context of the nonlinear results that we have reported in this paper, we note that cross-equatorial propagation might be inhibited if the westerlies were only weak (as is observed) and therefore wave-breaking occurred in these regions as a result of finite wave amplitudes. Nonlinear reflection might well occur in such cases, although there might also be nonlinear radiation into the opposite hemisphere if there were neighboring westerlies there. Another such ingredient is the Hadley circulation. Not only will the meridional component of the velocity tend to oppose the propagation of stationary Rossby waves to low latitudes (Watterson and Schneider 1987), but the Hadley circulation may act to maintain the low-latitude gradients of PV, thus violating one of the key assumptions required for the KM bound and hence inhibiting reflection. Nonconservative effects associated with the Hadley cell may also inhibit reflection by acting directly to dissipate wave activity at low latitudes. Some of the effects of the Hadley circulation have been considered by Held and Phillips (1990), who studied the interactions of a stationary Rossby wave with a zonally symmetric Hadley circulation in a single-layer model. It will potentially be of great interest to expand on their work, both in generalizing some of the assumptions made and in taking advantage of the finite-amplitude, wave-activity diagnostics in analyzing numerical results. This will be a priority for future studies.

A final important ingredient is the effect of synoptic-scale eddies. As noted in the introduction, there has been much interest in the interaction between synoptic-scale eddies and the larger-scale waves that are the focus of study in this paper. Such interaction may be important for the low-latitude absorption–reflection. The sort of numerical experiments reported by Cook and Held (1992), where topographic forcing is applied to excite large-scale waves in a GCM that otherwise has no imposed longitudinal asymmetries, might be one approach to investigating this issue.

*Acknowledgments.* We are grateful to Grant Branstator and three anonymous reviewers for useful comments that improved the manuscript. We thank Lois Steenman-Clark and Carl Friche for facilitating computer access. This work was supported by NSF Grant ATM-9615864, by NERC Grant GR3-8105, by the Isaac Newton Institute, and by the University of California, Irvine, through an allocation of computer time at the San Diego Supercomputer Center.

## REFERENCES

Ambrizzi, T., and B. J. Hoskins, 1997: Stationary Rossby-wave propagation in a baroclinic atmosphere. *Quart. J. Roy. Meteor. Soc.,* **123,** 919–928.

Andrews, D. G., and M. E. McIntyre, 1978: An exact theory of nonlinear waves on a Lagrangian-mean flow. *J. Fluid Mech.,* **89,** 609–646.

Branstator, G., 1983: Horizontal energy propagation in a barotropic atmosphere with meridional and zonal structure. *J. Atmos. Sci.,* **40,** 1689–1708.

——, 1992: The maintenance of low-frequency, atmospheric anomalies. *J. Atmos. Sci.,* **49,** 1924–1945.

Brunet, G., and P. H. Haynes, 1996: Low-latitude reflection of Rossby wave trains. *J. Atmos. Sci.,* **53,** 482–496.

Cook, K. H., and I. M. Held, 1992: The stationary response to large-scale orography in a General Circulation Model and a linear model. *J. Atmos. Sci.,* **49,** 525–539.

Edmon, H. J., B. J. Hoskins, and M. E. McIntyre, 1980: Eliassen–Palm cross-sections for the troposphere. *J. Atmos. Sci.,* **37,** 2600–2616.

Esler, J. G., 1997: Wave packets in simple equilibrated baroclinic systems. *J. Atmos. Sci.,* **54,** 2820–2849.

Grose, W. L., and B. J. Hoskins, 1979: On the influence of orography on the large-scale atmospheric flow. *J. Atmos. Sci.,* **36,** 223–234.

Haynes, P. H., 1988: Forced, dissipative generalizations of finite-amplitude wave-activity conservation relations for zonal and nonzonal basic flows. *J. Atmos. Sci.,* **45,** 2352–2362.

——, 1989: The effect of barotropic instability on the nonlinear evolution of a Rossby wave critical layer. *J. Fluid Mech.,* **207,** 231–266.

——, and M. E. McIntyre, 1987: On the representation of Rossby-wave critical layers and wave breaking in zonally truncated models. *J. Atmos. Sci.,* **44,** 2359–2382.

——, and W. E. Ward, 1993: The effect of realistic radiative transfer on potential vorticity structures, including the influence of background shear and strain. *J. Atmos. Sci.,* **50,** 3431–3453.

Held, I. M., 1985: Pseudomomentum and the orthogonality of modes in shear flows. *J. Atmos. Sci.,* **42,** 2280–2288.

——, and P. J. Phillips, 1990: A barotropic model of the interaction between the Hadley cell and a Rossby wave. *J. Atmos. Sci.,* **47,** 856–869.

——, and M. J. Suarez, 1994: A proposal for the intercomparison of the dynamical cores of atmospheric general circulation models. *Bull. Amer. Meteor. Soc.,* **75,** 1825–1830.

Hoskins, B. J., and A. J. Simmons, 1975: A multi-layer spectral model and the semi-implicit method. *Quart. J. Roy. Meteor. Soc.,* **101,** 637–655.

——, and T. Ambrizzi, 1993: Rossby-wave propagation on a realistic longitudinally varying flow. *J. Atmos. Sci.,* **50,** 1661–1671.

Hsu, H.-H., B. J. Hoskins, and F.-F. Jin, 1990: The 1985/86 intraseasonal oscillation and the role of the extratropics. *J. Atmos. Sci.,* **47,** 823–839.

Kiladis, G. N., and K. M. Weickmann, 1992: Extratropical forcing of tropical Pacific convection during northern winter. *Mon. Wea. Rev.,* **120,** 1924–1938.

Killworth, P. D., and M. E. McIntyre, 1985: Do Rossby-wave critical layers absorb, reflect or over-reflect? *J. Fluid Mech.,* **161,** 449–492.

Magnusdottir, G., and P. H. Haynes, 1996: Wave-activity diagnostics applied to baroclinic-wave life cycles. *J. Atmos. Sci.,* **53,** 2317–2353.

McIntyre, M. E., and T. G. Shepherd, 1987: An exact local conservation theorem for finite amplitude disturbances to non-parallel shear flows, with remarks on Hamiltonian structure and on Arnol'd's stability theorems. *J. Fluid Mech.,* **181,** 527–565.

Molteni, F., S. Tibaldi, and T. N. Palmer, 1990: Regimes in the wintertime circulation over northern extratropics. I: Observational evidence. *Quart. J. Roy. Meteor. Soc.,* **116,** 31–67.

Plumb, R. A., 1985: On the three-dimensional propagation of stationary waves. *J. Atmos. Sci.,* **42,** 217–229.

Randel, W. J., and D. L. Williamson, 1990: A comparison of the climate simulated by the NCAR Community Climate Model (CCM1:R15) with ECMWF analysis. *J. Climate,* **3,** 608–633.

Schubert, S. D., and C.-K. Park, 1991: Low-frequency intraseasonal tropical–extratropical interactions. *J. Atmos. Sci.,* **48,** 629–650.

Scinocca, J. F., and W. R. Peltier, 1994: Finite-amplitude wave-activity diagnostics for Long's stationary solution. *J. Atmos. Sci.,* **51,** 613–622.

Stewartson, K., 1978: The evolution of the critical layer of a Rossby wave. *Geophys. Astrophys. Fluid Dyn.,* **9,** 185–200.

Valdes, P. J., and B. J. Hoskins, 1988: Baroclinic instability of the zonally averaged flow with boundary layer damping. *J. Atmos. Sci.,* **45,** 1584–1593.

Wallace, J. M., and D. S. Gutzler, 1981: Teleconnections in the geopotential height field during the Northern Hemisphere winter. *Mon. Wea. Rev.,* **109,** 784–812.

——, and H.-H. Hsu, 1983: Ultra-long waves and two-dimensional Rossby waves. *J. Atmos. Sci.,* **40,** 2211–2219.

Warn, T., and H. Warn, 1978: The evolution of a nonlinear critical level. *Soc. Ind. Appl. Math.,* **59,** 37–71.

Watterson, I. G., and E. K. Schneider, 1987: The effect of the Hadley circulation on the meridional propagation of stationary waves. *Quart. J. Roy. Meteor. Soc.,* **113,** 779–813.

Waugh, D. W., L. M. Polvani, and R. A. Plumb, 1994: Nonlinear barotropic response to a localized topographic forcing: Formation of a ''tropical surf zone'' and its effect on interhemispheric propagation. *J. Atmos. Sci.,* **51,** 1401–1416.

Webster, P. J., and J. R. Holton, 1982: Cross-equatorial response to middle-latitude forcing in a zonally varying basic state. *J. Atmos. Sci.,* **39,** 722–733.

Yang, S., and W. J. Gutowski, 1994: GCM simulations of the three-dimensional propagation of stationary waves. *J. Climate,* **7,** 414–433.